Topographic Stability and Layer-Specific Flexibility are Mechanisms of Human Cortical Plasticity

Alicia Northall[1*], Juliane Doehler[1], Miriam Weber[2], Stefan Vielhaber[2], Stefanie Schreiber[2,3,4] & Esther Kuehn[1,3,4,5]

Author affiliations

[1] Institute for Cognitive Neurology and Dementia Research (IKND), Otto-von-Guericke University Magdeburg, Saxony-Anhalt, 39120, Germany

[2] Department of Neurology, Otto-von-Guericke University Magdeburg, Magdeburg, Saxony-Anhalt, 39120, Germany

[3] German Center for Neurodegenerative Diseases (DZNE), Magdeburg, Saxony-Anhalt, 39120, Germany

[4] Center for Behavioral Brain Sciences (CBBS) Magdeburg, Magdeburg, Saxony-Anhalt, 39106, Germany

[5] Hertie Institute for Clinical Brain Research, 72076 Tübingen, Germany

* indicates corresponding author

Alicia Northall: alicia.northall@med.ovgu.de

Institute for Cognitive Neurology and Dementia Research (IKND)

Leipzigerstrasse 44, 39120

Magdeburg, Saxony-Anhalt, Germany

Abstract

Age-related cortical plasticity reveals insights into the mechanisms underlying the stability and flexibility of neuronal circuits. Classical parcellation has long demonstrated the importance of microstructural features yet 3D approaches have rarely been applied to human brain organization *in-vivo*. We acquired functional and structural 7T-MRI and behavioral data of living younger and older adults to investigate human primary motor cortex (M1) aging, employing 3D parcellation techniques. We identify distinct cortical fields in M1 based on quantitative tissue contrast, which are, along with the myelin-poor borders between them, stable with age. We also show age-related iron accumulation, particularly in the output layer 5b and the lower limb field. Our data offers a new model of human M1 with distinct cortical fields, a mechanistic explanation for the stability of topographic organization in the context of aging and plasticity, and highlights the specific vulnerability of output signal flows to cortical plasticity.

Keywords: MRI, microstructure, motor cortex, cortical layers, aging, myelin, iron

Introduction

Age-related cortical plasticity reveals insights into the mechanisms underlying the stability and flexibility of neuronal circuits. For example, cortical thinning has been detected as a marker for aging, and has been used to understand different aspects of brain function such as use-dependent plasticity [1], learning [2], and disease [3]. Similarly, the concepts of enlarged cortical representations and de-differentiation have been identified as aging mechanisms [4], which have been used not only to understand human and animal aging [5]–[8], but also adaptive and maladaptive plasticity [9], [10].

Classical parcellation has long highlighted the importance of microstructural properties, such as layer-specific myelin and iron for functional brain organization [11], [12]. The important feature of parcellation-based analyses is that the cortex is investigated point-by-point along the cortical surface, as well as in depth, resulting in microstructural profiles that characterize the cortex in unprecedented detail. This has been referred to as three-dimensional (3D) modeling of the cortex [13], and has been used to parcellate cortical and subcortical structures of single individuals [14]. However, such approaches have so far rarely been applied to investigate *in-vivo* human brain organization in relation to plasticity, aging, or disease, and thus to understand the living human cortex in its full complexity.

Here, we used the primary motor cortex (M1) of younger and older adults as a model system to describe basic mechanisms of human age-related plasticity, by applying 3D parcellation-inspired techniques to *in-vivo* group data. Laminar variations in microstructure are particularly relevant for M1, since it is characterized by a prominent output layer 5 containing heavily-myelinated Betz cells, that are responsible for motor control via its projections to the effectors [15]. Superficial layers, on the other hand, connect to the premotor cortex, somatosensory cortex and other neighboring cortical areas and integrate planned motor commands into actions. Variations along the cortical surface are also relevant for M1, given its inhomogenous microstructural architecture where myelin-poor boundaries separate major body part

representations, such as the hand and face [16], [17]. Parcellation-based analyses are well-suited to investigate such variations across the cortical surface and with depth in living individuals. We utilized recent advances in ultra-high field MRI at 7-Tesla (7T-MRI) to obtain submillimeter resolution structural data, and combine them with functional localizers and behavioral assessments of motor function. We then applied parcellation-based analyses to in-vivo human group data to characterize the basic mechanisms of age-related motor plasticity.

More precisely, we describe the microstructural properties of M1 by using *in-vivo* proxies for myelin, iron, and diamagnetic substance/calcium in a sample of 20 younger and 20 older adults. To answer the question as to whether M1 can be regarded as a single cortical field (as for example suggested by Brodmann, [11]), or whether it is composed of several cortical fields (as for example suggested by Flechsig, [12]), we compared the MRI-based microstructural tissue profiles between the major body part representations of the face, upper limb, and lower limb. Note that previous research has detected myelin-poor borders between major body part representations and therefore indicated separation, but did not investigate whether the tissue contrast itself would differ between these areas [16], [17], therefore leaving the question open as to whether these areas should be classified as cortical fields. We further investigated whether these cortical areas, and the boundaries between them, would remain stable with age or whether they would show age-dependent plasticity. This is the first time that the stability of features defined by cortex parcellation has been investigated in living younger versus older adults. Finally, we investigated 3D iron depositions in M1, since age-related iron accumulation is widely evidenced [18]–[20] but has rarely been precisely localized. We specifically investigated whether age-related iron accumulation is pronounced in input-related structures, output-related structures, or would be homogenous across both. This insight provides important information on whether the connection between neighboring cortical areas and M1, or between M1 and effectors is most affected by age-related plasticity, and provides important information on the underlying cytoarchitecture.

To the best of our knowledge, this is the first study that has applied recently validated techniques of 3D *in-vivo* cortex parcellation [21]–[23] to group human brain data, to understand fundamental aspects of human brain organization in the context of age-related plasticity. The results of this study highlight the importance of using 3D models of cortical architecture to link brain structure to function.

Results

Extracting 3D Structural Profiles of M1

We quantified the cortical microstructure of M1 using quantitative T1 (qT1) as a proxy for cortical myelin content [21], positive-QSM (pQSM) as a marker for cortical iron content [22], and negative-QSM (nQSM) as a measure of cortical diamagnetic substance/calcium [23]. All three contrasts had a submillimeter resolution of 0.5-mm isotropic and therefore allowed us to characterize intracortical contrast with high precision and reliability (see **Fig. 1**). Given the known correlations between curvature and layer-wise qT1 values [24] (see **Fig. 1C** for our data), we followed a previous approach to regress out effects of curvature on qT1 values at each layer [24], resulting in 'decurved qT1' values (see **Fig. 2D**). We then applied a data-driven approach [25] to divide the depth of M1 into four anatomically-relevant compartments that we refer to as 'layers' (Ls = superficial layer; L5a = layer 5a; L5b = layer 5b; L6 = layer 6; see **Fig. 2E**). It should be noted that there is a conceptual difference between the layer definition applied here and the layer definition based on *ex-vivo* data, where cellular architectures are considered [11], [26]. Nevertheless, our approach was developed based on a comparison between *in-vivo* and *ex-vivo* M1 data [25], and therefore provides a reasonable approximation to describe input- and output-specific structures and their underlying computations [27].

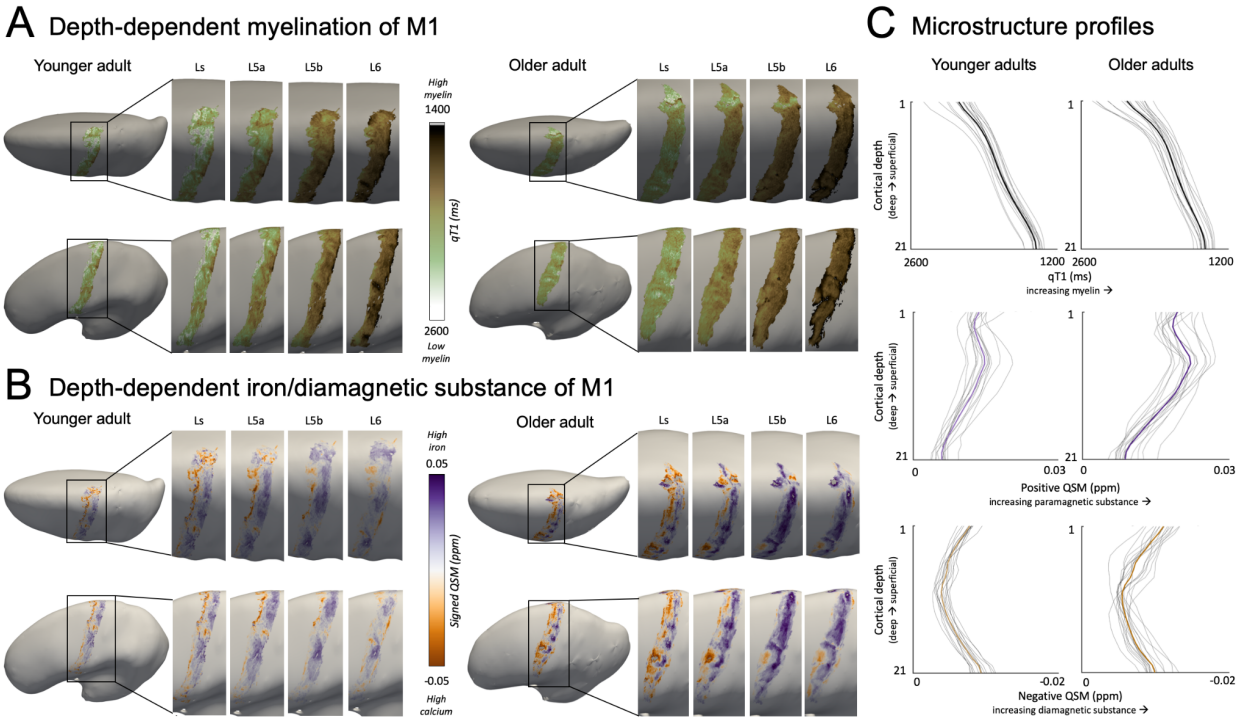

Figure 1. Extracting 3D structural profiles of primary motor cortex (M1). (A) Mapped qT1 values in M1 at each of the four anatomically-relevant cortical compartments ('layers') (Ls - superficial layer, L5a - layer 5a, L5b - layer 5b, L6- layer 6) for one example younger adult and one example older adult. (B) Mapped signed QSM values in M1 at each of the four anatomically-relevant cortical compartments ('layers'), for one example younger adult and one example older adult. Note that positive QSM values represent iron, whereas negative values reflect diamagnetic substance/calcium (C) 'Raw qT1' (i.e., not 'decurved qT1') profiles, positive QSM profiles, and negative QSM profiles for younger and older adults mapped at 21 cortical depths; the group mean is shown in bold color whereas individual data are shown in gray, purple, and black respectively.

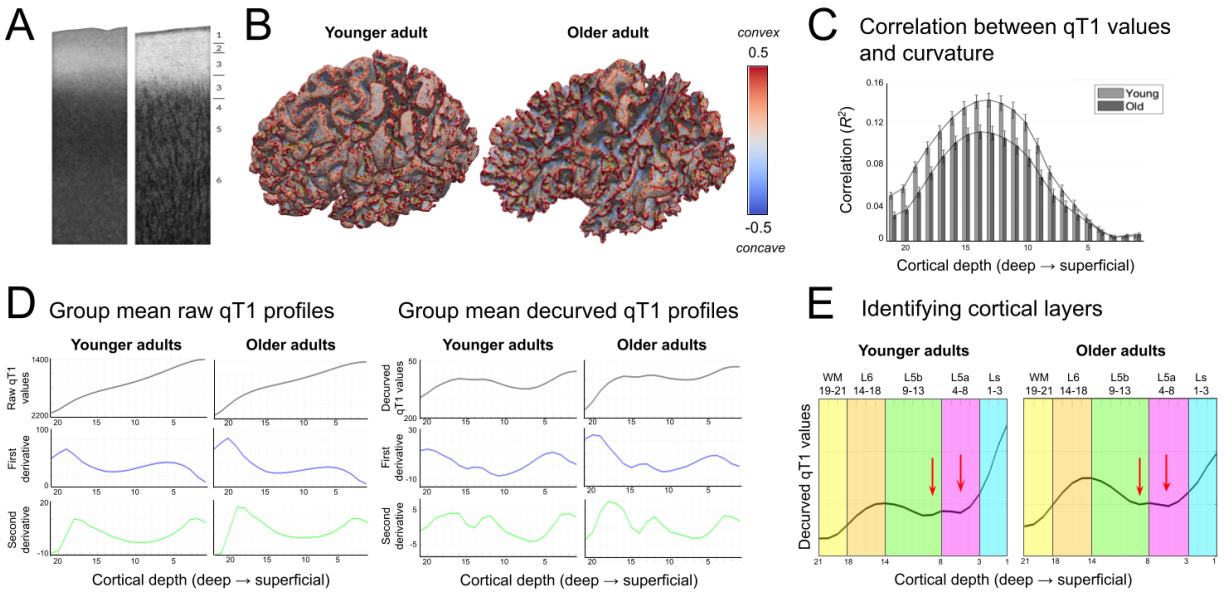

Figure 2. Identifying anatomically-relevant cortical compartments in M1. (A) Schematic depictions of M1 myelin (*left*) and cell histological staining (*right*) from [28] and [26]. (B) Mapped mean cortical curvature for one example younger adult and one example older adult. (C) Cortical depth-wise correlations between qT1 values and mean curvature for younger adults (*light gray*) and older adults (*dark gray*). Note that 21 correlations are shown because for initial data extraction, 21 depths were extracted. (D) Group mean 'raw qT1' and 'decurved qT1' profiles, along with their first and second derivatives. These profiles were used to define anatomically-relevant cortical compartments, here referred to as 'layers', based on an existing approach [25]. (E) The data-driven approach to identify 4 anatomically-relevant compartments ('layers') following a previously published approach [25] applied to 'decurved qT1' (Ls - superficial layer; L5a - layer 5a; L5b - layer 5b; L6 - layer 6). L5a and L5b were distinguished based on the presence of two small qT1 dips at the plateau of 'decurved qT1' values (indicating L5), while L6 was identified based on a sharp decrease in values before a further plateau indicating the presence of white matter. Please note that these cortical layers are defined based on *in-vivo* MRI data and may not correspond exactly to the anatomical layers as defined by ex vivo myelo- and cytoarchitecture. Also note that here, low qT1 values represent high myelin whereas in the other graphs in the article, values are plotted reversed such that high values represent high myelin; this approach was chosen here to allow an easy comparison with our layer definition to the previously published approach [25].

M1 Can be Divided into Distinct Cortical Fields

Next, we addressed whether M1 should be regarded as a single cortical field (as suggested by Brodmann, [11]), or whether it is composed of several cortical fields (as suggested by Flechsig, [12]). It has previously been reported that the face (F), upper limb (UL) and lower limb (LL) areas in M1 are separated by myelin-poor borders [16], [17]. However, it has not yet been investigated whether the microstructure between these areas also significantly differs, which is necessary to conclude that they are separate cortical fields, each with a distinct tissue composition. To investigate this, we computed ANOVAs with the within-subjects factors topographic area (F, UL, LL) and layer (Ls, L5a, L5b, L6) on qT1 and nQSM values as *in-vivo* proxies of cortical myelin and diamagnetic tissue contrast/calcium content, respectively. Note that only data of younger adults are reported in this section, since the aspect of the stability / flexibility of the tissue composition was investigated as a separate question (see below).

With respect to qT1 values, there are significant main effects of layer ($F_{(1.17,\ 18.63)} = 576.42$ and $P < 10^{-16}$) and topographic area ($F_{(1.30,\ 20.83)} = 5.34$ and $P = .024$), as well as a significant interaction between layer and topographic area ($F_{(2.12,\ 33.98)} = 12.78$ and $P < 10^{-5}$, see **Supplementary Table 1** for right hemisphere). The main effect of layer was expected and is driven by a significant decrease in qT1 values (i.e., an increase in cortical myelin) with cortical depth that is due to the high myelination in the deep cortex near the white matter [28]. More specifically, Ls shows higher qT1 values than L5a (Ls = 2083.17 ± 115.92; L5a = 1898.49 ± 72.21; t = 14.60, P < 10^{-10}), L5a shows higher qT1 values than L5b (L5b = 1743.68 ± 54.60; t = 21.59, P < 10^{-13}), and L5b shows higher qT1 values than L6 (L6 = 1569.05 ± 61.75; t = 36.41, P < 10^{-17}). The main effect of topographic area is due to significantly lower qT1 values in the LL area compared to the UL area (LL = 1818.24 ± 73.04; UL = 1824.57 ± 72.48; $t = -3.87$, $P = .001$) and significantly lower qT1 values in the LL area compared to the F area (F = 1827.97 ± 73.90; $t = -2.96$, $P = .009$). The significant interaction between layer and topographic area is driven by the LL area showing significantly lower qT1 values than the F area in L6 (LL = 1560.76 ± 63.27; F = 1582.22 ± 60.91; $t =$

-6.03, $P < 10^{-5}$) and the UL area showing significantly lower qT1 values than the F area in L6 (UL = 1564.16 ± 62.64; t = -4.22, P = .001). Additionally, the LL area shows significantly lower qT1 values than the UL area in Ls (LL = 2078.64 ± 115.98; UL = 2084.85 ± 113.79; t = -2.15, P = .047), L5a (LL = 1894.08 ± 71.82; UL = 1902.77 ± 72.26; t = -5.41, $P < 10^{-5}$) and L5b (LL = 1739.48 ± 54.64; UL = 1746.50 ± 54.63; t = -4.87, $P < 10^{-4}$). See **Supplementary Table 2** for post-hoc tests for right hemisphere.

With respect to nQSM values, there are significant main effects of layer ($F_{(1.41,\ 18.35)}$ = 235.32 and $P < 10^{-13}$) and topographic area ($F_{(2,\ 26)}$ = 5.05 and P = .014), but there is no significant interaction between layer and topographic area ($F_{(2.5,\ 32.50)}$ = 1.50 and P = .235, see **Supplementary Table 3** for right hemisphere). Note that more negative nQSM values reflect more diamagnetic tissue contrast [23]. The main effect of layer is driven by Ls showing lower nQSM values (i.e., more diamagnetic tissue) than L5a (Ls = -.0130 ± .0016; L5a = -.0088 ± .0013; t = -20.81, $P < 10^{-11}$) and L5a showing lower nQSM values than L5b (L5b = -.0055 ± .0008; t = -19.55, $P < 10^{-11}$), while L5b does not show significantly different values than L6 (L6 = -.0060 ± .0008; t = 1.78, P = .098). The main effect of topographic area is due to significantly lower nQSM values in the F area compared to the LL area (F = -.0086 ± .0008; LL = -.0081 ± .0011; t = -2.58, P = .023) and the UL area (UL = -.0083 ± .0010; t = -2.17, P = .049). See **Supplementary Table 4** for post-hoc tests for right hemisphere.

Taken together, we show that the F, UL and LL areas of M1 show significant differences in quantitative tissue contrast, which are typically used in classical parcellation. These differences are sometimes layer-specific (e.g. the hand area shows high myelin in L6 and the face area shows high myelin in L5a, the face area also shows high diamagnetic tissue contrast/calcium in deep layers) and sometimes occur as an effect across layers (e.g. the face area shows high iron across layers). Our results indicate systematic, and partly layer-specific, differences in the microstructural profiles of the F, UL and LL areas, thus we

refer to these areas as 'cortical fields' in the following text (i.e., F field, UL field, LL field). See **Fig. 3D** for a summary of the microstructural architecture of M1 in younger adults.

Topographic Stability Characterizes Human M1 Aging

Next, we investigated whether or not the three cortical fields identified above (i.e., F field, UL field, LL field) are stable with age, or show age-related plasticity. This is critical to investigate, given that the stability and flexibility of topographic architectures is often debated in the fields of aging, plasticity, and disease [29]. We calculate ANOVAs on qT1 and nQSM values with the factors cortical field (F, UL, LL), layer (Ls, L5a, L5b, L6) and age (younger, older). Overall, we replicate the qT1 differences between cortical fields across age groups (see details below), but, we critically do not find a significant interaction between age and cortical field or between age, layer and cortical field on qT1 values (interaction between age and cortical field: $F_{(2, 33)} = 2.22$ and $P = .117$; interaction between age, layer, and cortical field: $F_{(6, 198)} = 1.18$ and $P = .320$) or nQSM values (interaction between age and cortical field: $F_{(2, 28)} = .60$ and $P = .550$; interaction between age, layer, and cortical field: $F_{(6, 168)} = .20$ and $P = .977$). Please note that also for the right hemisphere, no such interactions were found (see **Supplementary Table 5** and **Supplementary Table 7**).

More specifically, an ANOVA with the factors cortical field (UL, LL, F), layer (Ls, 5a, 5b, 6) and age (younger, older) on qT1 values revealed significant main effects of layer ($F_{(1.18, 38.90)} = 781.22$ and $P < 10^{-28}$) and cortical field ($F_{(2, 66)} = 3.67$ and $P = .031$), as well as a significant interaction between layer and cortical field ($F_{(2.34, 77.04)} = 15.75$ and $P < 10^{-7}$, see **Fig.3A** and see **Supplementary Table 5** and **Supplementary Fig.3A** for right hemisphere). As expected, the main effect of layer is driven by a significant decrease in qT1 values with cortical depth, where Ls shows higher qT1 values than L5a (Ls = 2088.64 ± 138.93; L5a = 1876.59 ± 83.43; $t = 17.02$, $P < 10^{-18}$), L5a shows higher qT1 values than L5b (L5b = 1720.50 ± 67.50; $t = 30.14$, $P < 10^{-26}$), and L5b shows higher qT1 values than L6 (L6 = 1559.86 ±

65.59; $t = 34.81$, $P < 10^{-28}$). The main effect of cortical field is driven by significantly lower qT1 values in the LL field compared to the UL field (LL = 1807.69 ± 83.83; UL = 1813.76 ± 85.63; $t = -3.18$, $P = .003$). The significant interaction between layer and cortical field is driven by the LL field showing significantly lower qT1 values than the UL field in L5a (LL = 1873.29 ± 82.67; UL = 1882.57 ± 85.57; $t = -4.50$, $P < 10^{-5}$) and L5b (LL = 1716.51 ± 68.02; UL = 1724.45 ± 68.12; $t = -5.06$, $P < 10^{-3}$), and the LL field showing significantly lower qT1 values than the F field in L6 (LL = 1553.19 ± 66.60; UL = 1570.33 ± 65.46; $t = -5.85$, $P < 10^{-6}$) across age groups. In addition, the F field shows significantly lower qT1 values than the UL field in L5a (F = 1873.90 ± 83.39; UL = 1882.57 ± 85.57; $t = -3.09$, $P = .004$), while the opposite effect is present in L6 where the UL field shows significantly lower values than the F field (UL = 1556.08 ± 66.30; F = 1570.33 ± 65.46; $t = -5.76$, $P < 10^{-6}$). See **Supplementary Table 6** for post-hoc tests for right hemisphere.

The same ANOVA on nQSM values shows significant main effects of layer ($F_{(1.19, 33.41)} = 169.24$ and $P < 10^{-15}$) and cortical field ($F_{(2, 56)} = 9.42$ and $P < 10^{-4}$), as well as a significant interaction between layer and cortical field ($F_{(2.45, 68.45)} = 3.60$ and $P = .025$, see **Fig. 3C** and see **Supplementary Table 7** and **Supplementary Fig. 3C** for right hemisphere). The main effect of layer reflects a U-shaped curve in nQSM values with cortical depth, where Ls shows lower nQSM values than L5a (Ls = -.0133 ± .0019; L5a = -.0092 ± .0017; $t = -35.59$, $P < 10^{-25}$) and L5a shows lower nQSM values than L5b (L5b = -.0064 ± .0013; $t = -12.58$, $P < 10^{-13}$), while L5b shows higher nQSM values than L6 (L6 = -.0076 ± .0022; $t = 3.99$, $P < 10^{-4}$). The main effect of cortical field is driven by the F field showing significantly lower nQSM than the UL field (F = -.0093 ± .0014; UL = -.0091 ± .0015; $t = -2.48$, $P = .019$), and the F field showing significantly lower nQSM than the LL field (LL = -.0089 ± .0013; $t = -3.78$, $P = .001$), while the UL field shows significantly lower values than the LL field ($t = -2.30$, $P = .029$). The significant interaction between layer and cortical field on nQSM values reveals that this effect is confined to L6 of M1, where the F field shows significantly lower nQSM values than the UL field (F = -.0080 ± .0024; UL

= -.0076 ± .0023; t = -3.86, P = .001), the F field shows significantly lower nQSM values than the LL field (LL = -.0072 ± .0022; t = -3.88, P = .001), and the UL field shows significantly lower values than the LL field (t = -2.32, P = .028). In L5b, the F field shows significantly lower nQSM values than the UL field (F = -.0066 ± .0013; UL = -.0063 ± .0013; t = -3.22, P = .003) and the LL field (LL = -.0063 ± .0012; t = -3.40, P = .002), but the UL field does not show significantly different values compared to the LL field (t = -.92, P = .365). See **Supplementary Table 8** for post-hoc tests for right hemisphere.

In regards to age differences, there is a main effect of age on nQSM values ($F_{(1,28)}$ = 12.88 and P = .001), which is driven by significantly lower values (i.e., more diamagnetic tissue contrast/calcium) in older adults compared to younger adults across all cortical fields in M1 (younger adults = -.0083 ± .0001, older adults = -.0098 ± .0013, t = 3.59, P = .001). There is also a significant interaction between layer and age ($F_{(1.19,\ 28)}$ = 6.19 and P = .014), revealing that older adults show lower nQSM values (that is, more diamagnetic tissue contrast/calcium) compared to younger adults specifically in L5b (older adults = -.0072 ± .0011; younger adults = -.0055 ± .0084; t = 4.61, $P < 10^{-5}$, g = 1.72) and L6 (older adults = -.0091 ± .0021; younger adults = -.0060 ± .0001; t = 5.57, $P < 10^{-5}$, g = 2.18, see **Fig. 5B**). Note that we do not find significant effects of age for the right hemisphere (see **Supplementary Table 7**).

Taken together, we show age-related accumulation of diamagnetic tissue contrast/calcium in all cortical fields but specifically in the output layers 5b and 6 of dominant (left) M1, but we do not find age-related differences in myelin or diamagnetic tissue contrast/calcium between cortical fields in M1; we replicate the microstructural differences between cortical fields in older adults that we had already detected in younger adults' M1 (see previous section).

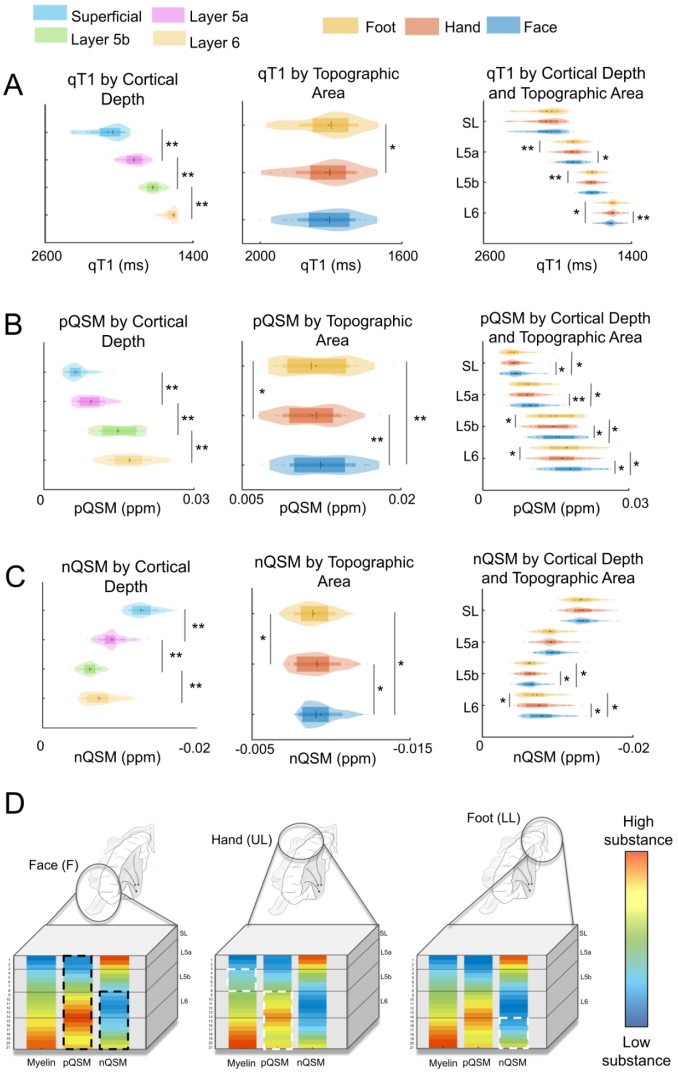

Figure 3. Topographic 3D Model of Human M1. Layer- and body part-specific effects on (A) qT1 values as a proxy for cortical myelin content [21], (B) pQSM values as a proxy of cortical iron content [22], and (C) nQSM values as a measure of diamagnetic tissue contrast [23]. (D) Overview of the 3D microstructural architecture of cortical fields in M1, highlighting which microstructural features characterize the face (F), upper limb (UL) and lower limb (LL) fields. Black dotted boxes indicate that the highlighted cortical field contains the highest substance compared to the other two fields; white dotted boxes indicate that the highlighted cortical field contains the lowest substance compared to the other two fields. When one cortical field only showed higher / lower substance in relation to one (but not both) other field, this is not highlighted here. * and ** indicate significance at the .05 and .001 p-value levels, respectively.

Hand-Face Myelin Border is Stable in Older Adults

Previous evidence has revealed that there are myelin-poor borders between the hand and face representations in younger adults [16], [17] which may indicate cortical separation [30]. The question as to whether or not these borders change with age reveal critical insights into the stability and flexibility of cortical representations. To test this, we compared averaged qT1 values sampled in the UL and F fields with the averaged qT1 value sampled at the F-UL-border, at each layer, between younger and older adults. We did not find significant age differences in any layer (Ls: t = 1.85, P = .073, L5a: t = 1.30, P = .203, L5b: t = -.03, P = .975, L6: t = -.01, P = .989, see **Fig. 4A**), where the Bonferroni-corrected threshold is P = .013 (note that we also do not find such differences in the right hemisphere, see **Supplementary Table 9** and **Supplementary Fig.4A**).

To investigate functional dedifferentiation of adjacent body part representations with age, we additionally calculated the mean dice coefficient of the overlap between the functional localisers of the UL and F areas [31]. We compared the dice coefficients between younger and older adults and found no significant differences when the representations where thresholded at different levels (threshold of .02: t = -1.83, P = .079, threshold of .04: t = -1.77, P = .088, threshold of .06: t = -1.77, P = .088, threshold of .08: t = -1.78, P = .087)), where the Bonferroni-corrected threshold is P = .013 (see **Fig. 4B**). However, all p-values were below 0.1, which indicates a statistical trend.

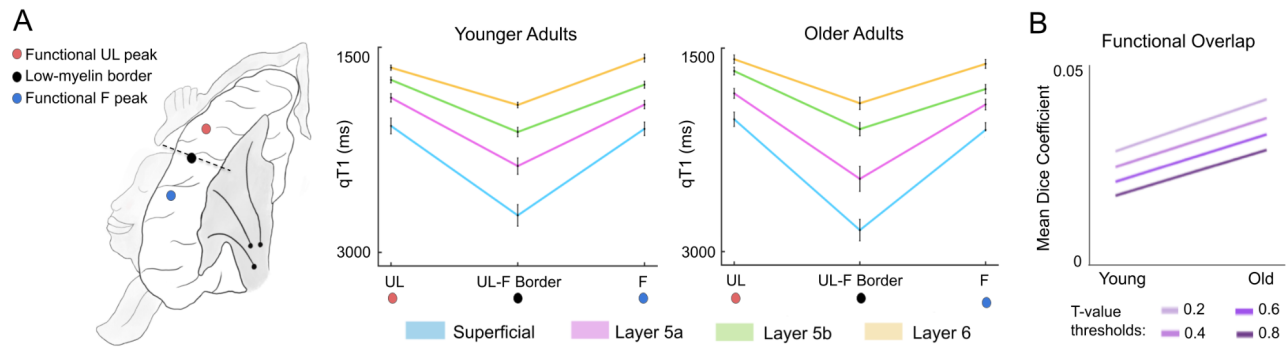

Figure 4. Hand-face myelin border is stable in older adults. (A) Layer-wise low-myelin (high qT1 value) border between the cortical fields of the upper limb (UL) and face (F) for both younger and older adults. In each group, we compare the mean body part qT1 values (hand+face/2) with the qT1 values at the hand-face border across layers. (B) Mean dice coefficients of the overlap between F and UL areas for younger and older adults, using different t-value thresholds to restrict the size of the functional representations.

3D Iron Accumulation in Older Adults' M1

Previous evidence shows that age-related iron accumulation [18]–[20] is a marker of maladaptive cortical aging [32]. To investigate whether iron accumulation in older adults' M1 would be particularly found in the input layers, output layers, or homogenous across layers, we performed an ANOVA with the factors cortical field (F, UL, LL), layer (Ls, L5a, L5b, L6) and age (younger, older) on pQSM values that served as a proxy for cortical iron content [22].

As expected, there is a significant main effect of age on pQSM values ($F_{(1,28)}$ = 56.24 and $P < 10^{-8}$), reflecting significantly higher pQSM values (i.e., more iron) in older adults compared to younger adults across M1 (older adults = .0143 ± .0019; younger adults = .0095 ± .0016; t = -7.50, $P < 10^{-8}$, see **Fig.5A** and see **Supplementary Table 11** and **Supplementary Fig.4B** for right hemisphere). However, there is also a significant interaction between layer and age on pQSM values ($F_{(1.31, 28)}$ = 8.88 and $P < .003$), which is driven by older adults showing the strongest effect size (highest Hedge's g), that is, most iron accumulation in L5b (older = .0178 ± .0023; younger = .0117 ± .0023; t = -7.42, $P < 10^{-8}$, g = 2.72, see

Fig.5A & 5D). There is also a significant interaction between age and cortical field on pQSM values ($F_{(2, 28)} = 3.89$ and $P < .026$), revealing that older adults show the strongest effect size, that is highest iron accumulation, in the LL field (F field: older = .0149 ± .0020; younger = .0100 ± .0018; $t = -7.24$, $P < 10^{-8}$, $g = 2.66$, UL field: older = .0137 ± .0018; younger = .0093 ± .0017; $t = -6.92$, $P < 10^{-7}$, $g = 2.54$, LL field: older = .0144 ± .0021; younger = .0092 ± .0016; $t = -7.56$, $P < 10^{-8}$, g = 2.81) (see **Fig.5A & 5E**). See **Supplementary Table 13** for post-hoc tests for right hemisphere. Note, however, that this topographic-specific iron accumulation is not present in the right hemisphere, while the layer-specific effect is also found in the right hemisphere. For the additional results of the ANOVA, see **Table 1** and **Table 2** (see **Supplementary Table 12** and **Supplementary Fig.3B** for right hemisphere).

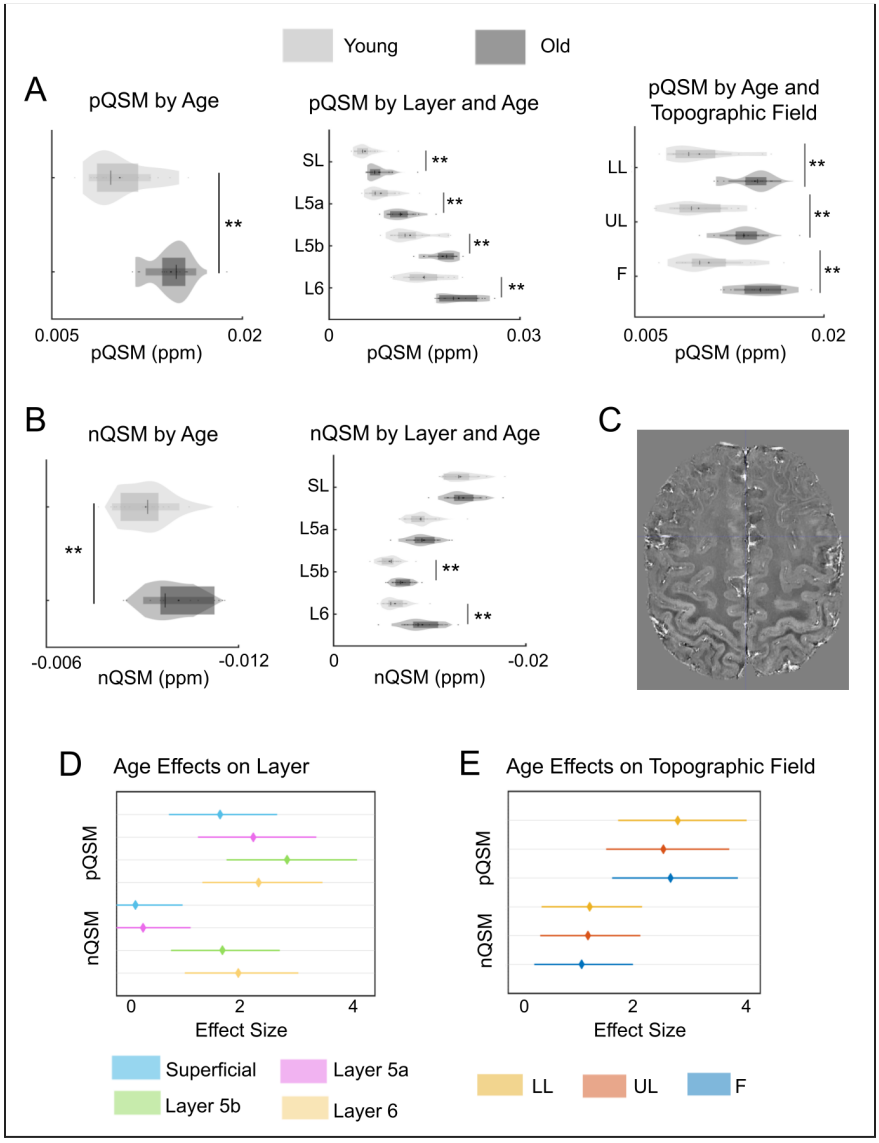

Figure 5. 3D Iron and Diamagnetic Tissue contrast/calcium Accumulation in M1. (A) Significant main effect of age, and significant interactions between layer and age, and between age and cortical field on pQSM values. (B) Significant main effect of age and significant interaction between age and layer on nQSM values. (C) Example whole-brain QSM image for a single participant. (D) Effect sizes for the age effects on layer QSM values, while (E) shows effect sizes for the age effects on cortical field QSM values. (Ls = superficial layer; L5a = layer 5a; L5b = layer 5b; L6 = layer 6). * and ** indicate significance at the .05 and .001 p-value levels, respectively.

Factor	*df*	Sum of squares	Mean square	*F*	*p*
Layer	1.31	.006	.002	299.99	10^{-21}**
Cortical area	2	10^{-5}	10^{-5}	22.17	10^{-8}**
Layer x cortical area	2.44	10^{-5}	10^{-6}	9.80	10^{-5}**

Table 1. Main effects of layer and cortical area, and the interaction between layer and cortical area on pQSM values in younger (n=14) and older (n=16) adults. * and ** indicate significance at the .05 and .001 p-value levels, respectively.

Pair	Paired differences				
	df	Mean difference	Standard deviation	*t*	*Sig.*
Main effects (layer, cortical area)					
Ls-L5a	29	-.0029	.0012	-14.76	10^{-15}**
L5a-L5b	29	-.0054	.0018	-16.87	10^{-16}**
L5b-L6	29	-.0023	.0017	-7.44	10^{-8}**
F-UL	29	.0010	.0009	5.88	10^{-6}**
UL-LL	29	-.0004	.0009	-2.39	.024*
LL-F	29	-.0006	.0007	-4.75	10^{-5}**
Interaction (layer-cortical area)					
Ls: F-UL	29	.0004	.0010	2.21	.035*
Ls: UL-LL	29	.0001	.0011	.67	.506
Ls: LL-F	29	-.0005	.0011	-2.73	.011*
L5a: F-UL	29	.0007	.0008	4.67	10^{-5}**
L5a: UL-LL	29	-.0001	.0011	-1.14	.264
L5a: LL-F	29	-.0005	.0009	-3.06	.005*
L5b: F-UL	29	.0014	.0012	6.12	10^{-6}**
L5b: UL-LL	29	-.0006	.0011	3.13	.004*
L5b: LL-F	29	-.0007	.0009	-4.22	10^{-4}**
L6: F-UL	29	.0016	.0013	6.75	10^{-7}**
L6: UL-LL	29	-.0009	.0010	-4.86	10^{-5}**
L6: LL-F	29	-.0007	.0011	-3.53	.001*

Table 2. Post-hoc t-tests for significant ANOVA effects on pQSM values in younger (n=14) and older (n=16) adults. (Ls = superficial layer; L5a = layer 5a; L5b = layer 5b; L6 = layer 6). * and ** indicate significance at the .05 and .001 p-value levels, respectively.

Taken together, we here show that iron accumulation in older adults' M1, which is regarded as a marker for maladaptive plasticity in aging [32], is particularly pronounced in the output layer 5b, suggesting output layer-specific iron accumulation in older adults' M1.

Body Part-Specific Motor Impairments in Older Adults

We also quantified body part specific motor functions in younger and older adults. More specifically, we investigated tongue kinematics using an automated tongue tracker (TT) [33] for F function, hand strength and dexterity [34] for UL function, and walking distance [35] for LL function. We find that older adults walked shorter distances than younger adults, and showed lower hand strength and poorer performance on pegboard tasks, and fewer tongue movements compared to younger adults (see **Fig. 6** for further details and statistics).

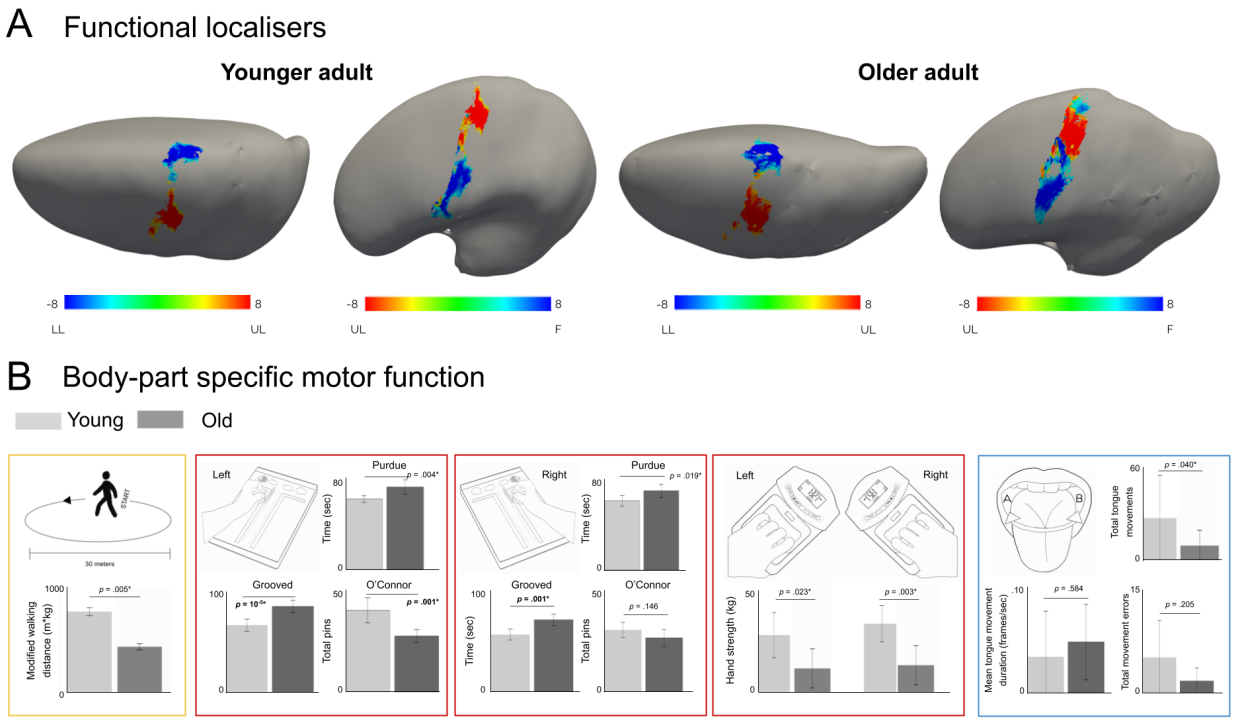

Figure 6. Body part-specific motor impairments in older adults. (A) Functional localisers of large-scale body part representations (LL = lower limb; UL = upper limb; F = face) in M1 for one example younger adult and one example older adult. (B) Body part specific tests of motor function (LL = 6MWT; UL = Purdue, Grooved and O'Connor pegboards; UL = Hand dynamometer; F = Automated tongue tracker) with group differences shown in bar plots. * indicates significance at the .05 p-value level, while bold values indicate significance at the Bonferroni-corrected threshold (p = .003).

Discussion

Age-related cortical plasticity reveals insights into the mechanisms underlying the stability and flexibility of neuronal circuits. 3D parcellation has long demonstrated the importance of microstructural features [11], [12] yet has rarely been applied to understand human brain plasticity and aging *in-vivo*. We here use the aging human M1 as a model system to study the 3D microstructural features of age-related plasticity, by applying parcellation-inspired techniques to sub-millimetre structural MRI data acquired in healthy younger and older adults. We show systematic differences in quantitative tissue contrasts between the M1 representations of the face (F), upper limb (UL), and lower limb (LL), which leads us to define them as distinct cortical fields. We demonstrate that these fields, along with the myelin-poor borders between them, remain stable with age, while iron and diamagnetic substances/calcium accumulate with age, particularly in the deeper layers of M1. Interestingly, age-related iron accumulation in the dominant hemisphere is particularly prominent in the output layer 5b of M1, where the giant Betz cells are located. Behavioral analyses further reveal deteriorated motor functions in older adults in all three body parts. Taken together, we provide a novel model of the microstructural architecture of human M1, and argue that topographic stability as well as layer-specific substance accumulation are central mechanisms of cortical plasticity that help to explain prior findings in the areas of learning, deprivation, aging, and disease.

We show that the face, upper limb and lower limb areas of M1 show distinct microstructural profiles: the face area is particularly characterized by high iron content across cortical layers and high diamagnetic substance/calcium in the output layers (layer 5b, layer 6), the upper limb area is particularly characterized by low myelin content in layer 5a and low iron content in the output layers, while the lower limb area is particularly characterized by low diamagnetic substance/calcium in layer 6. These results challenge classical depictions of human M1 as a single cortical area [11] and show that M1 should be divided into distinct cortical fields [12], each with distinct microstructural properties. Because these tissue properties, in particular myelin and iron content, link to different features of the cortex, our results question current

approaches that take the hand area of M1 as a model system to study motor plasticity, aging, or learning [36], [37]. Our data rather suggest that each of these cortical fields should be treated separately, since plasticity and disease mechanisms may be distinct for each field. This has already been indicated by studies on M1 neurodegeneration where disease spread markedly differs depending on which body part is first affected [38]. Other than previously described for the primary somatosensory cortex of younger adults [39], [40], our findings indicate that plasticity and disease mechanisms in M1 may not transfer to other body parts.

We also show that the microstructural tissue properties that define each cortical field, as explained above, are stable across age groups. In addition, we show that the myelin-poor border that separates the hand from the face area in younger adults [16], [17] remains stable with age. This age-related topographic stability suggests that there are limits to cortical plasticity and cortical spread within M1 in both younger and older adults [41]. This provides a mechanistic explanation as to why topographical organization is often maintained after learning or with deprivation, such as in amputees [42], [43], and as to why body representations are often preserved in older age [44]. However, as these borders also differ between individuals, our findings open up the investigation of these borders as a possible mechanism in neurodegenerative diseases that involve topographical disease spread [45].

Interestingly, we provide evidence for layer-specific plasticity as a mechanism of cortical aging. While previous studies have shown that iron accumulates across the brain with age [18]–[20], our study is the first to show that this accumulation is cortical depth-dependent in M1. Note that these age-related and layer-specific differences in iron accumulation cannot be due to differences in layer width in older adults, since the size of the layer compartments was the same across age groups, even though these were defined separately for each group. We show that age-related iron accumulation occurs most strongly in what we defined as layer 5b of the left (dominant) hemisphere and layer 6 of the right (non-dominant) hemisphere.

Layer 5b has been identified as a critical location for disease onset mechanisms in neurodegenerative diseases affecting motor control [15], and forms a closed-loop circuit with layer 6 responsible for the output of motor function [25]. The pronounced accumulation of iron in these layers suggests a particular vulnerability of this circuit in older adults, which identifies the Betz cells as critical targets for intervention, not only in neurodegeneration, but also in healthy aging.

We additionally show that the accumulation of paramagnetic substance/calcium does not co-localize with cortical myelin content, or iron accumulation, which indicates that it reflects changes in calcium content with aging, which disrupt neurotransmission and increase the risk of calcium depositions in blood vessels [46]–[48]. While we show age-related iron accumulation in all layers of M1, we show that age-related calcium accumulation occurs only in the left (dominant) hemisphere and is specific to the output circuit of M1, which further leads us to suggest that M1 output signal flows are particularly affected by age-related plasticity. This also suggests that age-related increases in iron and calcium likely depend on different mechanisms and thus warrant different therapeutic routes for maladaptive plasticity and neurodegeneration. Taken together, these results suggest that output structures of M1 are more vulnerable to age-related iron and calcium accumulation than are input structures of M1, which suggests that the signal flow from M1 to effectors is more affected by age-related plasticity than is the signal flow from premotor or somatosensory cortex to M1. Our study highlights the importance of a 3D approach to cortical plasticity that recognises layers and topographic areas as functionally-relevant units [13].

Finally, we show that the LL field accumulates the most iron with age; this effect was restricted to the left (dominant) hemisphere. This indicates the existence of topographic-specific age-related plasticity in M1. This is of particular relevance for neurodegenerative diseases where topographic-specific iron accumulation has been linked to symptom severity in affected body parts [49], [50], and identified as a mechanism for topographical disease spread [45]. This finding may also explain why older adults often

show particularly deteriorated walking and balance behavior, which is critically associated with reduced independence and executive function in late life [51]. The collection of more extensive behavioral test batteries than were acquired here is needed to investigate topographic-specific aging in more detail.

Taken together, we present a novel model of the 3D microstructural architecture of human M1, inspired by recent advances in *in-vivo* cortical parcellation, and identify three distinct cortical fields. More extensive mapping studies are needed to investigate whether also the trunk area, for example, could be defined as a cortical field. We argue that topographic stability and layer-specific plasticity are two central mechanisms of cortical plasticity, that can be used to explain prior findings across the areas of aging, learning, deprivation, and neurodegeneration, and that inspire novel interventions and therapeutic approaches to improve motor function in maladaptive plasticity. Our 3D model provides novel, laminar-specific routes to navigate the complex microstructure of the cortex in the living human brain.

Methods and Materials

Participants

40 healthy volunteers composed of 20 younger adults (< 35 years of age; 8 female) and 20 older adults (> 70 years of age; 11 female) were enrolled in the present study. After data quality check (details see below), a total of 35 participants, including 17 younger adults (8 female) with a mean age of 24.65 years (*SD* = 2.69 years) and 18 older adults (11 female) with a mean age of 71.06 years (*SD* = 4.04 years) remained for analysis. Participants were recruited from the DZNE database in Magdeburg and were paid seven euros per hour for the behavioral tests, and 30 euros for each MRI session. All participants were right-handed and exclusion criteria included chronic illnesses, neurological medications, sensorimotor deficits and contraindications to 7T-MRI (e.g. tattoos, metallic implants, tinnitus). The study was approved by the local Ethics Committee and all participants gave written informed consent.

Procedure

Data acquisition took place between August 2016 and November 2021, and included two MRI scanning sessions and one behavioral session: (1) Structural MRI session, (2) Functional MRI session, (3) Motor behavior session.

MRI Data Acquisition

Structural MRI data were acquired with a 7T-MRI scanner equipped with a 24-channel head coil (MAGNETOM, Siemens Healthcare), located in Magdeburg, Germany. We collected two MP2RAGE, a Magnetisation Prepared 2 Rapid Gradient Echoes (MP2RAGE) sequences [52]. We obtained a MP2RAGE slab image (covering M1 and S1) with a 0.5mm isotropic resolution (208 transversal slices, repetition time = 4800 ms, echo time = 2.62 ms, inversion time TI1/TI2 = 900/2750 ms, field-of-view read = 224 mm, bandwidth = 250 Hz/Px, GRAPPA 2, flip angle = 5◦/3◦, phase oversampling = 0%, slice oversampling = 7.7%) and a whole-brain MP2RAGE image with an isotropic resolution of 0.7mm (sagittal slices, repetition time = 4800 ms, echo time = 2.01 ms, inversion time TI1/TI2 = 900/2750 ms, field-of view read = 224 mm, bandwidth = 250 Hz/Px, GRAPPA 2, flip angle = 5◦/3◦). We also collected a whole-brain susceptibility-weighted (SWI) image with a 0.5mm isotropic resolution (transversal slices, repetition time = 22 ms, echo time = 9 ms, field-of view read = 192 mm, bandwidth = 160 Hz/Px, GRAPPA 2, flip angle = 5◦/3◦). The total scan time for the structural MRI session (session (1)) was approximately 60 minutes.

During the functional MRI session (session (2)), functional and additional SWI data were collected. The same sequence and parameters as above were used to collect SWI slab images (covering M1 and S1) with a 0.5-mm isotropic resolution. In addition, we obtained whole-brain functional images with a 1.5mm isotropic resolution (81 slices, field-of-view read = 212 mm, echo time = 25 ms, repetition time = 2000 ms, GRAPPA 2, interleaved acquisition) using an EPI gradient-echo sequence.

Experimental Design

The functional imaging (session (2)) involved a blocked-design paradigm, where the participants were asked to move their left or right foot, left or right hand, or tongue. Participants were trained on the movements outside the scanner. Instructions were shown on a screen inside the scanner (gray background, black color). They were asked to prepare for movement (e.g. 'prepare right hand') before carrying out the movement (e.g. 'move right hand') for 12 seconds, followed by 15 seconds of rest. Each movement was repeated four times, resulting in a total of 20 trials. The total scan time for the MRI session (2) was approximately 90 minutes.

Image Processing

Data Quality Inspection

The MP2RAGE data of n=4 adults (n=3 younger, n=1 older) were excluded due to low signal-to-noise ratio (SNR) and severe truncation artifacts affecting M1, leaving a total of n=36 participants (n=17 younger, n=18 older) for the main analyses. In addition, the SWI data of n=5 adults (three younger, two older) were excluded due to severe motion and truncation artifacts affecting M1, leaving a total of 31 participants (14 younger, 16 older) for the SWI analyses.

Structural Preprocessing

Structural images were processed using CBS Tools (version 3.0.8) [53] implemented in MIPAV (version 7.3.0) [54]. We first registered the slab MP2RAGE image to the whole-brain MP2RAGE image using the 'Optimized Automated Registration' module in MIPAV and ANTs (version 1.9.x) [55]. Registration quality in the sensorimotor areas were checked by two independent raters before proceeding. The slab and whole-brain images were then merged, resulting in whole-brain images with improved resolution in the slab region. In MIPAV, the MP2RAGE skull stripping module was used to remove extra-cranial tissue and

the MP2RAGE dura estimation module was used to estimate the dura mater, which was manually refined in ITK-SNAP to remove all extracranial tissue. The topology-preserving anatomical segmentation (TOADS) algorithm [56] was used to segment the UNI images into different tissue types based on a voxel-by-voxel probability approach. The cortical reconstruction using implicit surface evolution (CRUISE) module was then used to estimate the boundaries between the WM and GM, and between the GM and CSF [57], resulting in levelset images. Using these images, we created masks of the cortex, adjusting the WM-GM boundary to ensure that the deep GM of M1 was included. We finally divided the cortex into three layers and used the surface mesh inflation module to inflate the middle layer only, to reduce the impact of segmentation issues (due to partial volume effects close to the CSF and WM boundaries) on the surfaces used for mapping.

SWI Processing

Quantitative Susceptibility Maps (QSM) were calculated using the QSMbox (version 2.0) [58]. The reconstructed QSM images were then registered to the merged qT1 images using the automated registration tool in ITK-SNAP (version 3.8.0), with manual refinement (prioritizing alignment in M1) where necessary. Registration quality between the QSM and MP2RAGE images was checked by two independent raters before proceeding. We separated the QSM data into positive-QSM (pQSM) and negative-QSM (nQSM) values following a previously described approach [19].

M1 Masks

ROI masks of M1 in both hemispheres were manually delineated using the MP2RAGE with the manual segmentation tool in ITK-SNAP. Based on anatomical landmarks, the M1 region was defined to include all relevant topographic areas (foot, hand, face/lips/tongue). The omega-shaped knob was used as a landmark of the hand area in M1 [59]. To include the face area, we masked slices ventral to the hand knob until the precentral sulcus was visible. To include the foot area, we masked slices dorsal to the hand

knob until the precentral sulcus was no longer visible. Since the foot area extends superiorly to the longitudinal fissure [60], we masked the paracentral lobule (PCL) while avoiding the supplementary motor area and the primary somatosensory cortex [61].

Surface Mapping

We divided the cortex into 21 layers according to the equivolume approach implemented in the volumetric layering module [62], [63], using the volume-preserving layering method with an outward layering direction. We then sampled qT1 and QSM values at each layer, before mapping the values onto inflated cortical surfaces using the surface mesh mapping module with the closest-point method.

Defining Cortical Layers

We calculated mean curvature using the simple curvature function in ParaView (version 5.8.0) and regressed this out of qT1 values for each layer following a previously published approach [24]. Using group averaged decurved qT1 profiles, we applied a data-driven approach to define anatomically-relevant cortical layers [25] (see **Fig. 1E**). Layer 5 (L5) was identified based on a plateau in decurved qT1 after a steep increase in decurved qT1, reflecting the sharp increase in myelin content from the superficial layers to the heavily-myelinated L5 (depths 4-13). In addition, layer 5a (L5a) (4-7) and layer 5b (L5b) (8-13) were distinguished based on the presence of two small qT1 dips that are assumed to represent the two layer compartments [25]. Consequently, all depths above L5a (1-3) were labeled as the superficial layer (Ls), which we suggest to include anatomical layers 3 and 4 but not layers 1 and 2, since the latter are particularly sparse and inaccessible with MRI (as shown by Huber, [25]). We further defined layer 6 (L6, 14-17) based on a sharp decrease in decurved qT1, (18-21) after which values plateaued again indicating the presence of WM.

Functional Data Processing

Functional data were preprocessed using SPM12, including smoothing with a Gaussian kernel of 2mm, slice-timing to correct for differences in image acquisition time between slices, and realignment to reduce motion-related artifacts. The functional volumes were averaged and manually registered, based on anatomical landmarks, to the qT1 images using ITK-SNAP. First-level analysis was used to generate t-statistic maps (t-maps) based on contrast estimates for each body part (e.g. left hand = [1 0 0 0 0]). The peak cluster of each t-map was saved as a binary mask. In the few cases the peak cluster only included the face area of one hemisphere (tongue movement typically showed a single peak cluster including the face area of both hemispheres), we included the largest cluster in the face area of the other hemisphere in the resulting peak cluster mask. The t-maps and peak cluster masks were then registered to the qT1 images in ANTs, using the registration matrices previously generated in ITK-SNAP, before being mapped onto the same inflated cortical surfaces as used for the structural data. We applied the binarised peak cluster masks to the t-maps to create functional localisers which contained values only in the peak cluster. We refined the localisers by removing overlapping voxels between different localisers, where the body part with the highest t-value retained the overlapping voxel (i.e., 'winner-takes-it-all' approach). These refined functional localisers (shown in **Fig. 6A**) were then binarised and multiplied with the layer-wise qT1 and QSM values, resulting in values for each topographic area at four different cortical depths.

Myelin Border Analysis

Based on previous evidence of myelin-poor borders between the hand and face areas of M1 [16], [17], we defined the myelin border based on the highest qT1 value (lowest myelin) between the locations of the peak t-values of the UL and F localisers (see **Fig. 4A**). We extracted the qT1 values at the border and calculated the average body part qT1 values (UL+F/2).

Behavioral Tests of Motor Function

A subset of 27 adults (12 younger, 15 older) underwent behavioral tests of motor function for the F, UL and LL body parts. An automated tongue tracking tool that we introduced previously, called Tongue Tracker (TT), was used to quantify kinematic features of the tongue based on short video clips of lateral tongue movement, as an estimate of face motor function [33]. Participants were instructed to open their mouth and move their tongue between their mouth commissures as fast as possible, while being video recorded for a minimum of five seconds of correct movement. TT automatically extracted the total number of tongue movements completed, the average duration of a tongue movement and the number of errors made by the participant. We used a dynamometer to measure hand strength twice in each hand, before averaging to result in one measurement per hand [34]**.** The 6-Minute-Walking-Test (6MWT) was used to measure walking distance as an estimate of gross motor function of the leg [35]. Participants were instructed to walk as far as possible around a 30-meter measuring tape in six minutes without speed-walking. The total distance walked was multiplied by weight in kilograms as previously reported [64].

Statistical Analysis

Statistical analyses were performed using IBM SPSS Statistics (version 26, IBM, USA). Mixed-effects ANOVAs were used to assess between-group (age group) and within-group (layer, topographic area) differences for each measure of cortical microstructure (qT1, pQSM, nQSM). Significant main effects and interactions of the ANOVAs were investigated using post-hoc tests. Two-tailed independent-samples t-tests were used to measure group differences in the size of the myelin border and in behavioral measures of motor function, while one-tailed independent-samples t-tests were used to measure group differences in the mean dice coefficient of the overlap between functional representations. The significance level for all statistical tests was set to the 5% threshold ($p < .05$) and the Bonferroni method was used to correct for multiple comparisons.

Data Availability

Anonymised data can be made available upon request.

Acknowledgements

We would like to thank Lilith-Sophie Lange for her support in data collection. This project was funded by the Else Kröner Fresenius Stiftung: 2019-A03 and the Deutsche Forschungsgemeinschaft (DFG): KU 3711/2-1, project number: 423633679 and Projektnummer 425899996 – SFB 1436.

Author Contributions

E.K., S.S. and M.W. designed the study. J.D., M.W. and A.N. collected the data. A.N. and J.D. completed the data processing. A.N. carried out the data investigation and statistical analysis. A.N. wrote the manuscript. J.D., E.K., S.S and M.W. reviewed and edited the manuscript. E.K., S.S. and S.V. supervised the study. All authors contributed to the article and approved the submitted version.

References

1. Bermudez, P., Lerch, J. P., Evans, A. C., & Zatorre, R. J. Neuroanatomical correlates of musicianship as revealed by cortical thickness and voxel-based morphometry. *Cereb. Cortex* 19 (7), 1583-1596 (2009).
2. Sale, M. V. et al. Brain changes following four weeks of unimanual motor training: Evidence from behavior, neural stimulation, cortical thickness, and functional MRI. *Hum. Brain Mapp.*, 38 (9), 4773-4787 (2017).
3. Verstraete, E. et al. Structural MRI reveals cortical thinning in amyotrophic lateral sclerosis. *J. Neurol. Neurosur. Psychiatry*, 83 (4), 383-388 (2012).
4. Cabeza, R. Hemispheric asymmetry reduction in older adults: the HAROLD model. Psychol. Aging, 17 (1), 85 (2002).
5. Cassady, K., Ruitenberg, M. F., Reuter-Lorenz, P. A., Tommerdahl, M., & Seidler, R. D. Neural dedifferentiation across the lifespan in the motor and somatosensory systems. *Cereb. Cortex*, 30 (6), 3704-3716 (2020).
6. Liu, P. et al. The organizational principles of de-differentiated topographic maps in somatosensory cortex. *Elife*, 10, e60090 (2021).
7. Bernard, J. A., & Seidler, R. D. Evidence for motor cortex dedifferentiation in older adults. *Neurobiol. Aging*, 33 (9), 1890-1899 (2012).
8. Schmolesky, M. T., Wang, Y., Pu, M., & Leventhal, A. G. Degradation of stimulus selectivity of visual cortical cells in senescent rhesus monkeys. *Nat. Neurosci.*, 3 (4), 384-390 (2000).
9. Heuninckx, S., Wenderoth, N., & Swinnen, S. P. Systems neuroplasticity in the aging brain: recruiting additional neural resources for successful motor performance in elderly persons. *J. Neurosci.*, 28 (1), 91-99 (2008).
10. Quartarone, A. et al. Abnormal associative plasticity of the human motor cortex in writer's cramp. *Brain*, 126 (12), 2586-2596 (2003).
11. Brodmann, K. *Vergleichende Lokalisationslehre der Grosshirnrinde in ihren Prinzipien dargestellt auf Grund des Zellenbaues* (Barth, Leipzig, 1909).
12. Flechsig, P. E. *Anatomie des menschlichen Gehirns und Rückenmarks auf myelogenetischer Grundlage (Vol. 1)* (G. Thieme, Leipzig, 1920).
13. Kuehn, E., & Sereno, M. I. Modelling the human cortex in three dimensions. Trends Cogn. Sci., 22 (12), 1073-1075 (2018).
14. Alkemade, A. et al. A unified 3D map of microscopic architecture and MRI of the human brain. *Sci. Adv.*, 8 (17), eabj7892 (2022).
15. McColgan, P., Joubert, J., Tabrizi, S. J., & Rees, G. The human motor cortex microcircuit: insights for neurodegenerative disease. *Nat. Rev. Neurosci.*, 21 (8), 401-415 (2020).
16. Kuehn, E. et al. Body topography parcellates human sensory and motor cortex. *Cereb. Cortex*, 27 (7), 3790-3805 (2017).
17. Glasser, M. F. et al. A multi-modal parcellation of human cerebral cortex. *Nature*, 536 (7615), 171-178 (2016).
18. Acosta-Cabronero, J., Betts, M. J., Cardenas-Blanco, A., Yang, S., & Nestor, P. J. In vivo MRI mapping of brain iron deposition across the adult lifespan. *J. Neurosci.*, 36 (2), 364-374 (2016).
19. Betts, M. J., Acosta-Cabronero, J., Cardenas-Blanco, A., Nestor, P. J., & Düzel, E. High-resolution characterisation of the aging brain using simultaneous quantitative susceptibility mapping (QSM) and R2* measurements at 7 T. *Neuroimage*, 138, 43-63 (2016).
20. Hallgren, B., & Sourander, P. The effect of age on the non‐haemin iron in the human brain. *J. Neurochem.*, 3 (1), 41-51 (1958).
21. Stüber, C. et al. Myelin and iron concentration in the human brain: a quantitative study of MRI contrast. *Neuroimage*, 93, 95-106 (2014).

22. Langkammer, C. et al. Quantitative susceptibility mapping (QSM) as a means to measure brain iron? A post mortem validation study. *Neuroimage*, 62 (3), 1593-1599 (2012).
23. Deh, K. et al. Magnetic susceptibility increases as diamagnetic molecules breakdown: myelin digestion during multiple sclerosis lesion formation contributes to increase on QSM. *J. Magn. Reson. Imaging*, 48 (5), 1281-1287 (2018).
24. Sereno, M. I., Lutti, A., Weiskopf, N., & Dick, F. Mapping the human cortical surface by combining quantitative T 1 with retinotopy. *Cereb. Cortex*, 23 (9), 2261-2268 (2013).
25. Huber, L. et al. High-resolution CBV-fMRI allows mapping of laminar activity and connectivity of cortical input and output in human M1. *Neuron*, 96 (6), 1253-1263 (2017).
26. Vogt, C., & Vogt, O. *Allgemeine Ergebnisse Unserer Hirnforschung (Vol. 21)* (Barth, Leipzig ,1919).
27. Persichetti, A. S., Avery, J. A., Huber, L., Merriam, E. P., & Martin, A. Layer-specific contributions to imagined and executed hand movements in human primary motor cortex. *Curr. Biol.*, 30 (9), 1721-1725 (2020).
28. Dinse, J. et al. A cytoarchitecture-driven myelin model reveals area-specific signatures in human primary and secondary areas using ultra-high resolution in-vivo brain MRI. *Neuroimage*, 114, 71-87 (2015).
29. Saadon-Grosman, N., Tal, Z., Itshayek, E., Amedi, A., & Arzy, S. Discontinuity of cortical gradients reflects sensory impairment. *PNAS*, 112 (52), 16024-16029 (2015).
30. Sereno, M. I. et al. (1995). Borders of multiple visual areas in humans revealed by functional magnetic resonance imaging. Science, 268(5212), 889-893.
31. Dice, L. R. Measures of the amount of ecologic association between species. *Ecology*, 26 (3), 297-302 (1945).
32. Sullivan, E. V., Adalsteinsson, E., Rohlfing, T., & Pfefferbaum, A. Relevance of iron deposition in deep gray matter brain structures to cognitive and motor performance in healthy elderly men and women: exploratory findings. *Brain Imaging Behav.*, 3 (2), 167-175 (2009).
33. Northall, A. et al. An Automated Tongue Tracker for Quantifying Bulbar Function in ALS. *Front. Neurol.*, 223 (2022).
34. Peolsson, A., Hedlund, R., & Öberg, B. Intra-and inter-tester reliability and reference values for hand strength. *J. Rehabil. Med.*, 33 (1), 36-41 (2001).
35. Enright, P. L. The six-minute walk test. *Respir. Care*, 48 (8), 783-785 (2003).
36. Masiero, S., & Carraro, E. Upper limb movements and cerebral plasticity in post-stroke rehabilitation. *Aging Clin. Exp. Res.*, 20 (2), 103-108 (2008).
37. Dumel, G. et al. Multisession anodal transcranial direct current stimulation induces motor cortex plasticity enhancement and motor learning generalization in an aging population. *Clin. Neurophysiol.*, 129 (2), 494-502 (2018).
38. Ravits, J. M., & La Spada, A. R. ALS motor phenotype heterogeneity, focality, and spread: deconstructing motor neuron degeneration. *Neurology*, 73 (10), 805-811 (2009).
39. Muret, D. et al. (2014). Touch improvement at the hand transfers to the face. Current Biology, 24(16), R736-R737.
40. Muret, D., & Dinse, H. R. Tactile learning transfer from the hand to the face but not to the forearm implies a special hand-face relationship. *Sci. Rep.*, 8 (1), 1-8 (2018).
41. Sereno, M. I. Plasticity and its limits. *Nature*, 435 (7040), 288-289 (2005).
42. Makin, T. R., & Bensmaia, S. J. Stability of sensory topographies in adult cortex. *Trends Cogn. Sci.*, 21 (3), 195-204 (2017).
43. Striem-Amit, E., Vannuscorps, G., & Caramazza, A. Plasticity based on compensatory effector use in the association but not primary sensorimotor cortex of people born without hands. *PNAS*, 115(30), 7801-7806 (2018).
44. Riemer, M., Wolbers, T. & Kuehn, E. Preserved multisensory body representations in advanced age. *Sci Rep,* 9 (1), 1-8 (2019).

45. Schreiber, S., Northall, A., Weber, M., Vielhaber, S., & Kuehn, E. Topographical layer imaging as a tool to track neurodegenerative disease spread in M1. *Nat. Rev. Neurosci.*, 22 (1), 68-69 (2021).
46. Khachaturian, Z. S. Calcium Hypothesis of Alzheimer's Disease and Brain Aging. *Ann. N. Y. Acad. Sci.*, 747 (1), 1-11 (1994).
47. Thibault, O. et al. Calcium dysregulation in neuronal aging and Alzheimer's disease: history and new directions. *Cell Calcium*, 24 (5-6), 417-433 (1998).
48. Toescu, E. C., & Verkhratsky, A. The importance of being subtle: small changes in calcium homeostasis control cognitive decline in normal aging. *Aging cell*, 6 (3), 267-273 (2007).
49. Costagli, M. et al. Magnetic susceptibility in the deep layers of the primary motor cortex in amyotrophic lateral sclerosis. *NeuroImage Clin.,* 12, 965-969 (2016).
50. Kwan, J. Y. et al. Iron accumulation in deep cortical layers accounts for MRI signal abnormalities in ALS: correlating 7 tesla MRI and pathology. *PloS One*, 7 (4), e35241 (2012).
51. de Bruin, E. D., & Schmidt, A. Walking behaviour of healthy elderly: attention should be paid. *Behav. Brain Funct.*, 6 (1), 1-8 (2010).
52. Marques, J. P. et al. MP2RAGE, a self bias-field corrected sequence for improved segmentation and T1-mapping at high field. *Neuroimage*, 49 (2), 1271-1281 (2010).
53. Bazin, P. L. et al. A computational framework for ultra-high resolution cortical segmentation at 7 Tesla. *Neuroimage*, 93, 201-209 (2014).
54. McAuliffe, M. J. et al. Medical image processing, analysis and visualization in clinical research. In Proceedings 14th IEEE Symposium on Computer-Based Medical Systems, 381-386 (2001).
55. Avants, B. B. et al. A reproducible evaluation of ANTs similarity metric performance in brain image registration. *Neuroimage*, 54 (3), 2033–2044 (2011).
56. Bazin, P. L., & Pham, D. L. Homeomorphic brain image segmentation with topological and statistical atlases. *Med. Image. Anal.*, 12 (5), 616-625 (2008).
57. Han, X. et al. CRUISE: cortical reconstruction using implicit surface evolution. *Neuroimage*, 23(3), 997-1012 (2004).
58. Acosta-Cabronero, J. et al. A robust multi-scale approach to quantitative susceptibility mapping. *Neuroimage*, 183, 7-24 (2018).
59. Yousry, T. A. et al. Localization of the motor hand area to a knob on the precentral gyrus. A new landmark. *Brain*, 120 (1), 141-157 (1997).
60. Penfield, W., & Rasmussen, T. *The Cerebral Cortex of Man: A Clinical Study of Localization of Function* (Macmillan, Oxford, 1950).
61. Spasojević, G., Malobabic, S., Pilipović-Spasojević, O., Djukić-Macut, N., & Maliković, A. Morphology and digitally aided morphometry of the human paracentral lobule. *Folia Morphol.*, 72 (1), 10-16 (2013).
62. Waehnert, M. D. et al. Anatomically motivated modeling of cortical laminae. *Neuroimage*, 93, 210-220 (2014).
63. Waehnert, M. D. et al. A subject-specific framework for in vivo myeloarchitectonic analysis using high resolution quantitative MRI. *Neuroimage*, 125, 94-107 (2016).
64. Bernstein, M. L. et al. (1994). Reanalysis of the 12-minute walk in patients with chronic obstructive pulmonary disease. Chest, 105(1), 163-167.